
PHYSICS PERCEPTION IN SLOSHING SCENES WITH GUARANTEED THERMODYNAMIC CONSISTENCY

A PREPRINT

Beatriz Moya

Aragon Institute in Engineering Research
University of Zaragoza
Zaragoza, Spain
beam@unizar.es

Alberto Badias

Aragon Institute in Engineering Research
University of Zaragoza
Zaragoza, Spain
abadias@unizar.es

David Gonzalez

Aragon Institute in Engineering Research
University of Zaragoza
Zaragoza, Spain
gonzal@unizar.es

Francisco Chinesta

ESI Group chair. PIMM Lab.
ENSAM Institute of Technology
Paris, France
francisco.chinesta@ensam.eu

Elias Cueto

Aragon Institute in Engineering Research
University of Zaragoza
Zaragoza, Spain
ecueto@unizar.es

September 28, 2021

ABSTRACT

Physics perception very often faces the problem that only limited data or partial measurements on the scene are available. In this work, we propose a strategy to learn the full state of sloshing liquids from measurements of the free surface. Our approach is based on recurrent neural networks (RNN) that project the limited information available to a reduced-order manifold so as to not only reconstruct the unknown information, but also to be capable of performing fluid reasoning about future scenarios in real time. To obtain physically consistent predictions, we train deep neural networks on the reduced-order manifold that, through the employ of inductive biases, ensure the fulfillment of the principles of thermodynamics. RNNs learn from history the required hidden information to correlate the limited information with the latent space where the simulation occurs. Finally, a decoder returns data back to the high-dimensional manifold, so as to provide the user with insightful information in the form of augmented reality. This algorithm is connected to a computer vision system to test the performance of the proposed methodology with real information, resulting in a system capable of understanding and predicting future states of the observed fluid in real-time.

Keywords Physics perception · thermodynamics-aware deep learning · GENERIC · sloshing

1 Introduction

World simulation—undertood as the emulation of real world events— recreates the response of an environment where a robot operates [1]. For AI-enabled robotics, these systems are crucial for emulating their sensing and understanding capacities to perform the mission they have been entrusted. Fluid manipulation is a rather difficult task to be accomplished, and trustable physics-based simulation of liquids is desired for success [2] [3] [4].

The merge of knowledge-driven and data-driven learning is settling in dynamical modeling, enabling the study of complex systems of highly non-linear nature [5]. This is known generally as “physics-informed deep learning”, although very different techniques may fall under this broad classification. Despite the common interest in introducing well-known physical knowledge into these approaches, there is a great divergence of proposals to be considered. From solving PDEs [6] [7] to learning constitutive laws based on invariants and conserved quantities [8] [9], these works establish a strong framework to work towards generalizable deep learning.

These techniques keep expanding but access to full sets of experimental variables are not always available. Some works propose to model fluid dynamics with data coming from images [10] [11] or sensors [12], but we take the risk of missing key information for the description. In contrast, there are proposals that intend to reconstruct the missing dynamical data. We propose an imaged-based method combined with physics knowledge to reconstruct the dynamical state of the fluid from the free surface detected in video frames. If the information comes from cameras in the form of video streams, this means that 30 to 120 frames per second will be available, and a similar feedback rate is expected for the system so as to transmit a smooth sensation to the user. Under such stringent rates, encoding the information available to a low-dimensional manifold is mandatory. By these means, we establish a bridge between real systems with their digital twins [13] [14].

The aim of the present work is to develop a system for fluid dynamics understanding and reasoning by means of data-driven modeling and simulation, whose result is thermodynamically admissible. The simulation engine is of course coupled with a computer vision system to build online digital twins of fluids. The performance of the loop must achieve real-time speed to guarantee a trustable decision making.

In our approach, the information we require for physics-informed prediction—not only position, but also velocity and stress fields and internal energy—is inaccessible to a commodity depth camera (we do not consider here more sophisticated systems such as particle image velocimetry, for instance). We hypothesize that the knowledge of the internal variables we need for a complete description of the fluid will come, on one hand, from the training with full-field computational data coming from simulations and, on the other, from the history of partial measurements performed during runtime. The information of the free surface is evaluated in sequences to distill the dynamical information needed from the time evolution of the surface. We use a recurrent neural network (RNNs) to reconstruct the dynamical state to perform adequate simulations and project the state of the fluid to a reduced-order space where simulations are performed to achieve real-time performance. On top of that, an augmented reconstruction is provided afterwards, outputting not only the state of the full fluid volume, but also velocity, internal energy, and stress fields that were not accessible in the first place.

To guarantee the thermodynamic admissibility of the resulting simulations, we actually learn from data a particular formulation of the dynamics based on the so-called General Equation for the Non-Equilibrium Reversible-Irreversible Coupling (GENERIC) formalism [15]. GENERIC constitutes a generalization of Hamiltonian dynamics to dissipative phenomena. Under the scope of GENERIC acting as an inductive bias [16], or learning constraint, during the learning procedure, we ensure the accomplishment of the basic principles of energy conservation and entropy generation, thus providing a physically sound learning framework.

The paper is structured as follows. Section 2 describes the state of the art with regard to recent works in the field. Section 3 describes the problem in detail. Section 4 discloses the method, from the projection of the dynamics to a lower dimensional manifold, to the physics learning and the connection with partial measurements. The training and implementation details are explained across section 5. Section 6 showcases the results obtained with real world measurements. We end up with a discussion of the results and an evaluation of the future developments that can derive from this work.

2 Works in the field

2.1 Self-supervised estimation of dynamical states

Labelling is an indisputable bottleneck for data-driven prediction. Thus, we need a background of understanding that substitutes the need of labeling, enabling machine self-intuition for deep understanding of the information available. This has a clear importance in robotics and visual perception and understanding based on images [4] [17] [18] [19]. Dynamical modeling, and specifically fluid dynamics, also need to tackle with this lack of information when performing experimental emulation and validation. Many internal variables employed in the descriptions are not easily measurable. Whereas some works carried out the modeling with regard to the information obtained from images [10] [11] or sensors [12], many agreed to reconstruct the dynamical internal state of the fluids for an accurate description [20]. Dynamics typically use strategically placed sensors that acquire data to recover the full set of quantities from sparse observations [21] [22]. A number of works employ deep neural networks (DNN) for this purpose. Erichson et al. [23]

claim the use of shallow neural networks for reconstructing fluid flows. Lye et al. [24] estimate the unknown input parameters in turbulent flows from observables.

Our contribution consists of a hybrid proposal between image and physics-based reconstruction by means of computer vision analysis.

2.2 Deep learning incorporating physics priors

In spite of the use of self-supervised learning to compensate the lack of unlabeled data, supervised methods still need a large database for learning a model. Few data could jeopardize the accuracy of the approximations. For instance, black-box schemes do not succeed at this task since very often not enough information is provided to learn global expressions and efficient generalizations [25]. Inductive biases [16] enforce the network to learn certain relationships on data to lead to a target function. On top of that, they contribute to reach convergence and reduce error bounds [26]. As a result, less data is required and the results are more realistic and accurate.

Physics-informed deep learning is a current trend in artificial intelligence. Many approaches have been released to leverage theoretical knowledge into the networks to improve the learning procedure [6] [27] [28]. Hamiltonian (thus, conservative) systems are regular test benchmarks for these techniques [29] [30]. Nevertheless, systems of utmost importance, such as those that involve Newtonian and non-Newtonian fluid dynamics, require beyond-equilibrium schemes. Thermodynamic neural networks constitute a framework that enables the study of any physical system, including those of inherent dissipative nature [31]. Yu et al. [32] apply the generalized Onsager principle to unveil the relationships among the state variables to ensure the fulfillment of the principle for a Runge-Kutta integration scheme. GENERIC [15] describes the evolution in time of a set of variables—that must be complete in the sense of being able to describe the energy of the system—with regard to the evolution of energy and entropy of the system under study. By learning the slow manifold of their evolution, the dynamics can be fully described at a coarse-grained scale [33]. This learning theory has been successfully applied to model rather different and complex behaviors [34] [35] [36] [37]. In recent works, it has been coupled with DNNs to build the so-called Structure Preserving Neural Networks (SPNN) [38] [39].

If we focus on the field of fluid simulation, DNNs are an extended tool for emulating their physics [40]. [41] [42] model fluid behavior by applying CNNs to model 2D and 3D fluid dynamics. In the case of [43], the authors distill the dynamics of unsteady flows with RNNs. Following the same spirit, [44] employ specifically LSTMs in reduced order manifolds. Recently, graph methods are becoming popular in this field [45]. With regard to physically informed deep learning, there are also works related to the study of fluids. [46] apply PINNs to high-speed flows. The work of [47] presents an approach to learn PDEs from Physics-informed CNNs. Particularly in the context of scene understanding and interaction with fluids, there exist plenty of approaches [45] [48] [49] [4]. In [50], the authors propose closing the learning loop with observations that help to correct the errors of the simulation, which is pursued with the implementation of Navier Stokes in conjunction with Smooth Particle Hydrodynamics [51]. In contrast, we propose a purely data-driven learning led by physical priors to simulate in a reduced order space and achieve both accuracy and generalization as well as real-time performance. We believe in the enforcement of the GENERIC formalism to discover fast and accurately the patterns of the dynamics for such perception and interaction tasks.

2.3 Computer vision in fluids estimation

Although the algorithm is trained with computational data, the final goal is to connect it with real liquids to close the perception loop. Detection and tracking of fluids, as well as containers, may be difficult if they lack of texture. The measurements obtained are usually invalid or noisy because the surfaces are not Lambertian [52]. We are interested in the detection of fluids, and particularly the free surface. [53] [50] propose the use of CNN to perform tracking of the fluids. In the work of [54], the authors propose an algorithm for filling level detection with RGB-D cameras. We propose an approach similar to the one presented in the work [55]. We convert the color image into a binary image in black and white to detect the color gradient that appears in the free surface.

3 Problem description

In this work we propose a strategy to train simulators for physical scene understanding. Similar strategies have been developed in recent times, see [49] for instance. However, in contrast with these works, we aim to develop a technique in which quantitative—and not only qualitative—information is given. This is of utmost importance if our perception system is to be employed in an industrial framework in the form of a digital twin of an asset, for instance. Thus, it is of primary importance to ensure that the learned simulator is able to make predictions that adhere to known basic principles of physics, such as the laws of thermodynamics.

We have considered the problem of fluid sloshing as a proof of concept for this analysis. This is in part due to its practical interest (to construct robots able to manipulate fluids, for instance) but also for its generality: sloshing is a (nonlinear) physical phenomenon that presents several interesting and challenging characteristics. Among them, a dissipative behavior. While there is a plethora of works devoted to learning conservative phenomena, based upon Hamiltonian or Lagrangian descriptions (see, among others, [9] [56] [57] [58] [59] [60]), very little has been investigated for learning dissipative phenomena.

We consider a system whose time evolution is described in terms of a set of state variables that ensure the full description of its thermodynamical state. In general, any physical system can be described at different levels (micro, meso, macro), that incorporate different information. At the molecular dynamics scale, physics are described by the positions and momenta of every molecule. While at this scale Newtonian laws apply and everything is conservative, the number of degrees of freedom, and also the time scale at which the phenomenon evolves, makes this type of description useless. Coarser levels incorporate less information, but also involve less degrees of freedom [61]. At this level, the effect of unresolved variables (those of lower levels not considered) on the evolution of resolved ones (those considered in the coarse level) introduces dissipation, by the celebrated fluctuation-dissipation theorem [62]. The presented approach aims to model Newtonian, and also non-Newtonian (shear-thinning) fluids at a hydrodynamics level that remain in a laminar regime. At hydrodynamics level, position, velocity, internal energy and stress fields are the state variables required for a full description of a (possibly non-Newtonian) fluid dynamics scenario in terms of the GENERIC formalism [63]. Thus, for a fluid discretized into M particles, the set \mathcal{S} of variables will be

$$\mathcal{S} = \{z = (\mathbf{r}_j, \mathbf{v}_j, E_j, \boldsymbol{\tau}_j, j = 1, 2, \dots, M) \in (\mathbb{R}^3 \times \mathbb{R}^3 \times \mathbb{R} \times \mathbb{R}^6)^M\}. \quad (1)$$

With the help of an RGBD camera, whose detailed description is carried out in Section 6.1, only partial measurements of these variables are observable. We are not interested in using complex laboratory equipments such as particle imaging velocimetry, for instance, that would greatly limit the generality of our approach. Instead, with the help of the camera we have access to the position of the free surface of the fluid at each frame, as will be detailed below. This severely limits the amount of information at our disposal, and obliges us to develop a system able to unveil hidden information of the dynamical state. In this sense, our methodology is somehow linked to (at least, partially) self-supervised methodologies.

As a proof of concept, we implement the learning algorithm to perceive the physics of different fluids contained in a glass subjected to arbitrary movements made with our hand. This phenomenon has been first reproduced computationally for different velocities so as to obtain time-discretized computational data of the fluid volume, which had previously been discretized into M particles. It has been computationally modeled and simulated by employing Smooth Particle Hydrodynamics [51]. We perform four simulations per fluid by applying four different initial glass velocities to trigger the dynamics. Then, we evaluate the state of the fluid at discretized time steps for each simulation. The required state variables are evaluated at each particle and stored for each time step. As a result, we have a collection of snapshots that describe the state of the fluid to perform training of the networks. Afterwards, the system must be able to predict and interpret the behavior of a glass under different, previously unseen, conditions with limited information.

4 Methodology and architecture

The complexity of the task just presented obliges us to implement our system in three different steps, see Fig. 1 for a graphical sketch of the implemented architecture. The highly dimensional nature of the problem motivates the reduction of the dynamics to carry out learning on an embedded space of much lower dimension. In the case of learning and predicting new situations from real world data, we need to establish a correlation between the data available (the free surface) and the latent space built from full computational descriptions. We hypothesize with the existence of features (distinctive attributes) in the data sequence that correlate these partial measurements with the history and internal variables of the fluid. An architecture based on recurrent neural networks can unveil the correlations and map the data acquired to the latent space, and output the reconstructed state in the next time step.

To accomplish these requirements, we need to develop three different architectures. Firstly, we have to project our computational data, with which we will train our simulator at step 1, to a lower dimensional manifold to train the algorithm efficiently and achieve real-time performance in the computation. As a second step, we work over an algorithm based on recurrent neural networks to substitute the encoder by a perceptron capable of projecting partial measurements to the latent space. Finally, we need to train a physics-informed integrator that will learn the evolution of the dynamics in the latent space. It is worth mentioning that, although we could have built a RNN autoencoder, we choose to proceed in two different steps and apply transfer learning. In transfer learning, the knowledge acquired training an algorithm is profited in a new application. Sloshing dynamics is already a complex problem to apply model order reduction, and working with limited information from the free surface could have complicated the learning process of learning a low dimensional manifold. In spite of this considerations, deep nets resulted from the training given the complexity of the patterns to learnt.

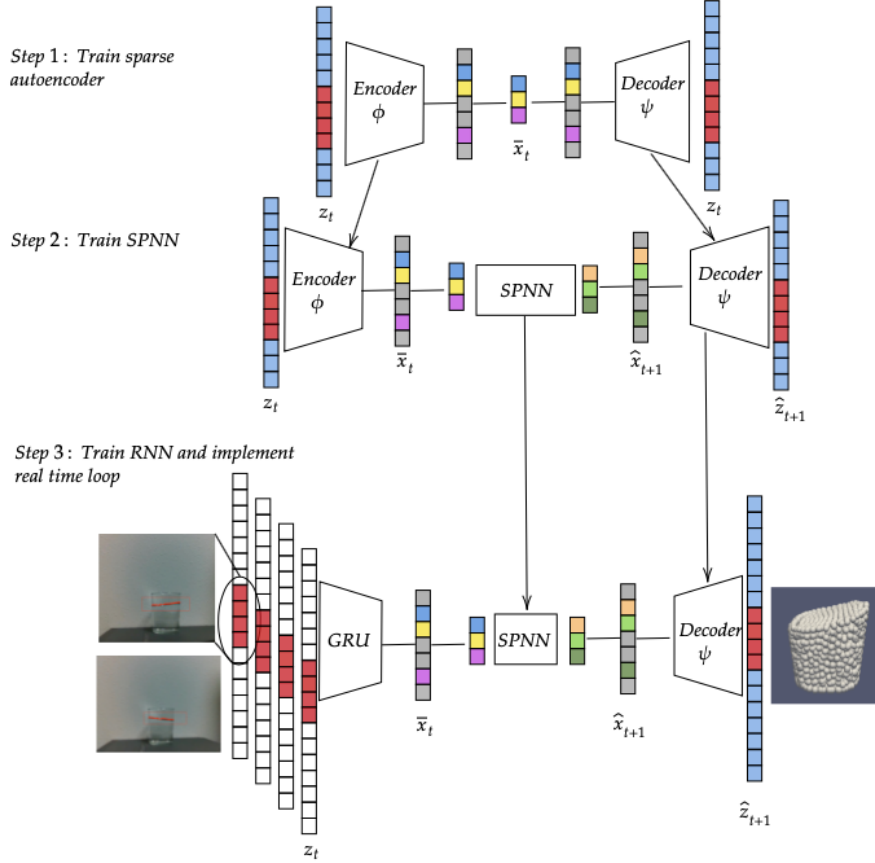


Figure 1: Sketch of the construction procedure for the deep neural network able to perceive sloshing phenomena. In a first step (first row), we must unveil the intrinsic dimensionality of the problem. To that end, we train a sparse autoencoder from computational full-field data. Once the number of variables governing the physics has been determined, we must train a structure-preserving neural network, able to integrate in time the state of the system. Thus, at step 2 in the figure, given the state of the system at time t , the decoder will output the state of system at time $t + \Delta t$. But the main difficulty is that during runtime we do not have access to the high-dimensional state of the system, only a portion of it, represented in red in the input vector of the network. These values correspond to the position of the free surface of the fluid. Thus, the encoder must be substituted in step 3 by a GRU that takes the near history of the free surface to convert it into the reduced-order encoding of the system that will feed the thermodynamics-informed time integrator.

4.1 Model reduction based on autoencoders

Despite the advances in terms of computational resources and calculation power, as well as capacity of storage, model order reduction is still a necessary tool to deal with the abundance of data and the physical complexity of certain phenomena. Training a complex database could truncate the convergence to an optimal result. Such is the case of the database available to build the model of the present work. In addition, operating on a low-dimensional manifold could also foster the robustness and stability of the proposed learning scheme so that changes in the input do not strongly condition the stability of the solution.

Currently, the development of these techniques is focused on capturing the important features of the non-linearities. Fluid dynamics are lead by strong non-linear structures hard to be learnt by machine learning methods. New approaches arise from the perspective of autoencoders [64] [65] as a preprocessing step to deal with turbulence and instabilities.

Given a set of snapshots that lives in a smooth finite-dimensional manifold $\mathcal{M} \in \mathbb{R}^D$, with $D = 13M$, as discussed in Eq. (1), we aim to find a projection to a manifold of latent variables $\mathcal{N} \in \mathbb{R}^d$ of much lower dimensionality, $d \ll D$. Autoencoders are an alternative to perform such reduction by finding patterns in the spatiotemporal structure of data. They are neural networks based on unsupervised learning. They consist of two parts, an encoder that maps data to an embedded space, and a decoder that reconstructs latent information to the original space. They set the target value of

the decoder $\hat{z}_t = \hat{z}(t)$ to be equal to the input $z_t = z(t)$, and backpropagate the loss to enhance the reconstruction,

$$\begin{aligned} \text{Encoder } \phi : \mathcal{M} \subset \mathbb{R}^D &\rightarrow \mathbb{R}^d \\ z &\mapsto x, \end{aligned}$$

$$\begin{aligned} \text{Decoder } \psi : \mathcal{N} \subset \mathbb{R}^d &\rightarrow \mathbb{R}^D \\ x &\mapsto \hat{z}. \end{aligned}$$

These schemes have shown good performance unveiling non-linear features to provide low and accurate representations. In this work, we have decided to use sparse autoencoders (SAE) so the sparsity in the bottleneck provides the real low dimensionality of the problem. This is accomplished automatically by the sparse autoencoder, by employing L1-norm penalization [66]. This can be interpreted, in the light of scientific machine learning, as a very practical form of imposing parsimony—in other words, Occam’s razor—to the learned model [8].

The backpropagated loss has two terms. With N_{snap} as the number of snapshots introduced in the algorithm, the first loss term $\mathcal{L}_{\text{mse}}^{\text{sae}}$ evaluates the reconstruction error between the ground truth and the result of the decoder,

$$\mathcal{L}_{\text{mse}}^{\text{sae}} = \frac{1}{N_{\text{snap}}} \sum_{i=1}^{N_{\text{snap}}} (z_i - \hat{z}_i)^2. \quad (2)$$

It is measured with the mean squared error (MSE) between the output and the input. Secondly, a regularizer term $\mathcal{L}_{\text{reg}}^{\text{sae}}$ is introduced to enforce the sparsity of the solution for the latent state snapshots x_i ,

$$\mathcal{L}_{\text{reg}}^{\text{sae}} = \sum_{i=1}^{N_d} |x_i|, \quad (3)$$

where N_d is the dimension of the latent vector of the autoencoder. This is fixed a priori as a big enough value, and the number of non-vanishing entries (i.e., the intrinsic dimensionality of data) will be determined without user intervention during the train period.

The regularization contribution is weighted with a coefficient $\lambda_{\text{reg}}^{\text{sae}}$ to control its influence in the training process,

$$\mathcal{L}^{\text{sae}} = \mathcal{L}_{\text{mse}}^{\text{sae}} + \lambda_{\text{reg}}^{\text{sae}} \mathcal{L}_{\text{reg}}^{\text{sae}}. \quad (4)$$

Although we have applied normalization over the dataset to perform learning, we decided to embed each group of state variables (position, velocity, internal energy, and stress tensor separated in normal σ and shear τ components) separately to capture all the important features of each group of variables. In other words, we define five different autoencoders. The latent variables coming from each autoencoder together will form the complete latent space of the dynamics. This decision has been taken for optimization and accuracy reasons. The five encoders to be defined have the same structure. The encoder and decoder have the same architecture, but inverted. They have been defined as fully connected and non recursive layers that follow a feed-forward scheme.

4.2 Recurrent neural networks for state reconstruction

The latent space is built from computational data obtained from simulations, for which we have a full description of the different fluid states. Computational data includes internal variables important in our description, whereas they are unmeasurable by ordinary means from camera inputs. We hypothesize that, although internal variables are not measurable, their influence can be unveiled from the dynamical evolution of the free surface. From this information, we could analyze the features of the history of the dynamics where these internal variables will arise.

Following the spirit of self-supervised learning, in the sense of unveiling not-given information, we propose an approach based on recurrent neural networks (RNNs) to reconstruct the state of the fluid. RNNs are structures that take into consideration the history of data since they work over sequences instead of learning from discrete and individual snapshots. RNNs are widely used, specially in the fields of natural language processing, speech recognition or economics. Vanilla RNN often encounter, however, vanishing and exploding gradient problems [67]. Gated Recurrent Units (GRU) [68] and Long Short-Term Memory (LSTM) units [69] are architectures capable of dealing with these problems. They include *gates*, or flows of information, to keep important information in long or complex sequences while forgetting irrelevant features.

The basic idea behind the GRU architecture is to accumulate information from previous layers, see Fig. 2. The hidden state h_t represents a kind of a summary of the features identified in previous sequences. g_t^{update} is the output of the

update gate. This gate selects which information from the hidden state and the input sequence passes to the next step, modeled with a sigmoid activation function. As it models the past information that must be considered into the future, it resembles to the information with regard to the internal variables that will influence the reconstruction. In contrast, the reset gate r_t reflects the past information that should be avoided. A new memory cell n_t is defined with regard to the reset information to store only the relevant information from the past. The output is the final hidden state h_t that accumulates the relevant information of past states and features learnt from the current input sequence:

$$\begin{aligned} g_t^{\text{update}} &= \sigma(\mathbf{x}_t U^z + \mathbf{h}_{t-1} W^z), \\ r_t &= \sigma(\mathbf{x}_t U^r + \mathbf{h}_{t-1} W^r), \\ n_t &= \tanh(\mathbf{x}_t U^h + (r_t \mathbf{h}_{t-1}) W^h), \\ \mathbf{h}_t &= (1 - g_t^{\text{update}}) \mathbf{h}_{t-1} + g_t^{\text{update}} n_t. \end{aligned}$$

GRUs have two main gates: an update gate, to update the hidden state, and a reset gate, which evaluates whether the previous cell state is relevant. In contrast with LSTMs, GRUs do not have a forget gate, which controls what is considered important to be remembered or to be rendered futile, and has less parameters. In spite of having a simpler structure, GRU's performance is similar to LSTM in certain tasks. In fact, GRUs have been proven to train faster and more efficiently with smaller datasets and shorter sequences [70].

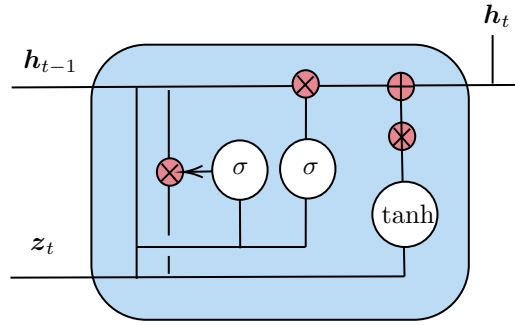


Figure 2: Representation of a GRU cell. The three main paths indicated represent the update and reset gates, the new memory cell, and their connection to update the new hidden state transmitted to the next later.

The input of the network consists of a sequence of measurements of the position of the free surface of the fluid. Since it is firstly trained with computational data, we select the particles of the discretization that belong to the free surface at each time step. The batch of sequences is introduced in the network to pass through GRU recurrent layers doing a projection *from-many-to-one*, i.e., introducing a sequence to obtain a single vector as output. The output vector of the GRU layers passes through a final forward fully connected layer with linear activation. The result of this process $\hat{\mathbf{x}}_t$ must match the latent state vector corresponding to the last snapshot \mathbf{x}_t of the given sequence. The loss $\mathcal{L}_{\text{mse}}^{\text{GRU}}$ evaluates the MSE between the predicted latent state and the ground truth,

$$\mathcal{L}_{\text{mse}}^{\text{GRU}} = \frac{1}{N_{\text{snap}}} \sum_{i=1}^{N_{\text{snap}}} (\mathbf{x}_i - \hat{\mathbf{x}}_i)^2. \quad (5)$$

4.3 Learning the dynamical evolution based on Structure Preserving Neural Networks

We have already mentioned the fact that one of our primary interests is to develop a technique that satisfies known basic principles of physics. Thus, the learnt time integrator should respect first principles of physics so as to provide credible predictions of future events to help in a decision making process. By structure-preserving neural networks (SPNN) we refer to a class of techniques that are constructed so as to satisfy some a priori known properties of the problem such as equivariance [71] or energy conservation [57] [60]. In their most general form, they can be applied to conservative as well as dissipative problems, in which the principles of thermodynamics are satisfied by construction [39] [38]. In the case of SPNN, we work from a thermodynamical perspective to drive learning through thermodynamically admissible scenarios that will ensure the consistency of the results. Therefore, we employ inductive biases that come from thermodynamic priors.

When the phenomenon at hand is dissipative, a particularly convenient formalism to describe its evolution in time is GENERIC. It presents a formulation to model the evolution of the vector of variables \mathbf{z} from the analysis of the energy

(Hamiltonian) potential in conjunction with a second (Massieu) potential that captures the dissipative nature of the dynamics. It is expressed in terms of Poisson and friction brackets, which can be reformulated as matrix operators, as

$$\frac{dz}{dt} = \mathbf{L}(z) \frac{\partial E(z)}{\partial z} + \mathbf{M}(z) \frac{\partial S(z)}{\partial z}. \quad (6)$$

The product of the gradient of energy and the symplectic matrix, $\mathbf{L}\nabla E$, models the conservative part of the time evolution, while the entropy gradient and the friction matrix $\mathbf{M}\nabla S$ capture the occurring dissipative effects beyond equilibrium. To discern which part of the evolution is governed by conservative phenomena and which one by dissipation, an additional condition must be imposed, the so-called degeneracy conditions,

$$\mathbf{L} \frac{\partial S}{\partial z} = \mathbf{0}, \quad \mathbf{M} \frac{\partial E}{\partial z} = \mathbf{0},$$

that state that energy has nothing to do with dissipation (it is conserved in closed systems) and entropy is not responsible of reversible phenomena.

In fact, these degeneracy conditions guarantee the conservation of energy,

$$\dot{E}(z) = \nabla E(z) \cdot \dot{z} = \nabla E(z) \cdot \mathbf{L}(z) \nabla E(z) + \nabla E(z) \cdot \mathbf{M} \nabla S(z) = 0, \quad (7)$$

and the production of entropy,

$$\dot{S}(z) = \nabla S(z) \cdot \dot{z} = \nabla S(z) \cdot \mathbf{L}(z) \nabla E(z) + \nabla S(z) \cdot \mathbf{M} \nabla S(z) \geq 0, \quad (8)$$

respectively.

These requirements are guaranteed if we choose \mathbf{L} and \mathbf{M} to be skew-symmetric and symmetric, positive semidefinite, respectively. For the sake of clarity, it is worth mentioning that GENERIC preserves these properties in the full-order as well as in the reduced-order manifold, enabling the learning of its structure in the latent space. In other words, it works equally well for z and x , provided that x represent well the dynamics.

We work on a discretized context of data samples, and learning is performed over a discrete expression of GENERIC. In this case, we consider a Forward Euler approximation of the time derivative that describes the dynamical evolution of the system. From this expression, the discrete degeneracy conditions to be imposed can be straightly derived:

$$\frac{x_{n+1} - x_n}{\Delta t} = \mathbf{L}(x_{n+1}) \mathbf{DE}(x_{n+1}) + \mathbf{M}(x_{n+1}) \mathbf{DS}(x_{n+1}), \quad (9)$$

where \mathbf{L} , \mathbf{M} , \mathbf{DE} and \mathbf{DS} represent the discretized versions of \mathbf{L} , \mathbf{M} , ∇E and ∇S , respectively, and the subscript n refers to time $t = n\Delta t$ and $n + 1$ indicates time $t + \Delta t$, respectively.

The SPNN follows a feed-forward flow which consists of a set of fully connected layers that learn the gradients of energy and entropy as well as the matrices \mathbf{L} and \mathbf{M} . The learning scheme enforces the skew-symmetry and symmetry of \mathbf{L} and \mathbf{M} respectively and the degeneracy conditions. Given pairs of consecutive snapshots, the neural network learns the integrator of the dynamical problem. The input is the state vector of latent variables at time t and $t + \Delta t$, x_n and x_{n+1} . The output coming from the net is a vector which contains the predicted \mathbf{L} , \mathbf{M} , and gradients of energy and entropy of the current state. During runtime, the time integration is consecutively performed with these operators.

The loss that carries the information to train and guide the SPNN is composed by two different terms. Firstly, the final output coming from the integration must match the ground truth. The accuracy is evaluated by measuring the mean squared error of these quantities,

$$\mathcal{L}_{\text{mse}}^{\text{SPNN}} = \frac{1}{N_{\text{snap}}} \sum_{i=1}^{N_{\text{snap}}} (x_i - \hat{x}_i)^2. \quad (10)$$

Secondly, training is also governed by the degeneracy conditions. They are taken into account as a loss coming from the sum of the squared values of both conditions,

$$\mathcal{L}_{\text{deg}}^{\text{SPNN}} = \frac{1}{N_{\text{snap}}} \sum_{i=1}^{N_{\text{snap}}} (\mathbf{L}_i \mathbf{DS}_i)^2 + (\mathbf{M}_i \mathbf{DE}_i)^2. \quad (11)$$

Finally, the MSE loss is weighted with the hyperparameter $\lambda_{\text{mse}}^{\text{SPNN}}$ to control its influence in the complete loss function of the network with regard to the problem,

$$\mathcal{L}^{\text{SPNN}} = \lambda_{\text{mse}}^{\text{SPNN}} \mathcal{L}_{\text{mse}}^{\text{SPNN}} + \mathcal{L}_{\text{deg}}^{\text{SPNN}}. \quad (12)$$

Table 1: Training parameters for each SAE.

| | lr | wd | λ^{sae} |
|----------------------------|-----------|-----------|------------------------|
| Position (q) | 10^{-4} | 10^{-6} | 10^{-3} |
| Velocity(v) | 10^{-4} | 10^{-5} | 10^{-3} |
| Internal energy (e) | 10^{-4} | 10^{-5} | 10^{-4} |
| Normal stress (σ) | 10^{-4} | 10^{-5} | 5×10^{-3} |
| Shear stress (τ) | 10^{-3} | 10^{-6} | 5×10^{-3} |

5 Training and validation

We train the algorithm from computational simulations performed in Abaqus CAE (Dassault Systèmes). It includes an add-on to perform conversion into particles and apply SPH in the simulations [72]. Each of the performed simulations are 2 seconds long, time at which the fluid reaches the equilibrium state. We evaluate the state of the fluid at discrete time steps, equally spaced by time increments of 0.005 seconds. As a result, we have 1600 snapshots available for training. This dataset is split in two subsets, 80% for training and 20% for test. The same training subsets are employed for training the three networks. The particles are labelled, and the data is stored for each time step into a vector following the order of the labelling. The geometry is not a parameter of the problem, and we have a constant discretization of the fluid. Nevertheless, the method is aimed to be able to learn the patterns of the dynamics, specially of those of the free surface, to emulate appropriately the sloshing perceived.

Once the three nets have been trained, we assemble the algorithm to feed the simulation loop with only a sequence of limited data. Instead of providing all the state variables obtained from the simulations, we pretend we have only measured the position at some points of the free surface. The sequence will be projected to the latent space, the SPNN will learn the dynamics, and the decoder will output results of the simulation augmenting the information originally given. The decoder provides the whole reconstruction of the fluid as well as the velocities, stresses and internal energy.

5.1 Hyperparameters and characteristics of each net

Each snapshot consists of a state vector of the position, velocity, internal energy and stresses (shear and normal) evaluated at each particle of the discretized fluid. The fluid is discretized in 2134 particles. Thus, the global dimensionality is 27742.

The SAE is subdivided in five different SAE, one for each subset of state variables. The nets have been initialized following the Kaiming method in which, briefly speaking, the weight initialization follows a Gaussian and biases are set to 0 [73]. In addition, we apply linear activations in the first and last layers, and ReLU for hidden layers. The optimizer chosen for these nets is Adam. A scheduler is programmed for updating the learning rate after 1000 and 3000 epochs.

We adapt the architectures according to the input dimension and their complexity or noisy nature of the values, and encoder and decoder have a symmetric structure:

- Position: Input size is $D = 6402$ and output size $d = 20$. It is composed by $N_h = 2$ hidden layers of size 120.
- Velocity: Given the complexity of the velocity, we built a net of input size $D = 6402$, output size $d = 20$, $N_h = 4$ hidden layers, and hidden size 200.
- Internal energy: In the case of energy, input size is $D = 2134$, output size $d = 10$, and there are $N_h = 3$ hidden layers which consist of 40 neurons each.
- Normal stress: The normal stress tensor components are identical. Thus, the input shape of the net is $D = 2134$, the output shape is $d = 20$, and it is composed of $N_h = 3$ hidden layers of 200 neurons.
- Shear stress: This net had input size $D = 6402$, $N_h = 3$ hidden layers of 200 neurons, and output size $d = 20$.

The specific learning parameters such as learning rate (lr), weight decay (wd) and sparse weights (λ^{sae}) are established individually for each SAE. Table 1 shows the parameters defined for each net. Given the complexity of the patterns learnt, we required low learning rates.

After 10000 epochs, SAEs converge to optimal results. Taking into account the sparsity imposed to improve the reduction, the final dimension of each net is $d_{\text{position}} = 3$, $d_{\text{velocity}} = 3$, $d_{\text{energy}} = 2$, $d_{\sigma} = 3$ and $d_{\tau} = 2$. Thus, the final shape of the reduced space is $d_{\text{latent space}} = 13$. The latents obtained are the output of the RNN, and the input of the

SPNN. This substantial reduction will not only reduce computing time and storage, but also improve the convergence to a solution in subsequent trainings.

The recurrent neural network relates partial measurements of the fluid to the latent space that we have built. We consider that the only information accesible by ordinary means in real time is information related to the free surface of the fluid. Specifically, we pretend we can only measure the position at some points of the free surface.

We take each full-order snapshot of the database to find the particles that represent the free surface of the liquid evaluating their height over their neighbors. Those points do not necessarily follow a balanced distribution, i.e. they are not uniformly distributed in the free surface. Given the density of the surface particle set, we simply perform linear interpolation to obtain a uniform free surface grid. This step facilitates comparison between sequences in future predictions. As a result, we have equally discretized free surfaces of 21 points, which results in a vector of size 42. In spite of reconstructing a 3D representation of fluids, we only consider a 2D data projection in the recurrent autoencoder to be consistent with the information that will come from the camera. Although the depth map of the images will be reconstructed, the measurements will still be noisy. Thus, we decided to rely on the 2D data, perpendicular to the depth, that will be more stable. This projection represents the coordinates of the surface in the direction of the movement, and their vertical height due to the sloshing effect.

Once we have the information related to the free surface at each time step, we create the sequences. We consider sequences of 16 snapshots. This parameter has been chosen from analyzing training results. It is the minimum sequence size to guarantee that the features of the dynamics are correctly captured. With smaller sequences, the RNN does not learn good projections to the latent space. Since it is a short, although complex, sequence, GRU is optimal for this case.

Even though the time step of the data in our database is 0.005 seconds, the camera we work with streams depth measurements at a frequency of 60 Hz. Therefore, to assemble the sequences, we must choose snapshots equally spaced by approximately 0.015 seconds.

The input size of the net is batch size \times sequence length \times vector size. The net consists of three GRU hidden layers of 26 neurons, and there is a last feed forward fully connected layer to connect the last GRU layer to the latent space of size 13. This last layer has linear activation. The optimizer for training this net is Adam, and parameters are set to $lr = 10^{-3}$, $wd = 10^{-5}$. The learning rate is updated by a scheduler at 1000 and 3000 epochs.

We reach good results after 10000 epochs. Training loss is 1.19×10^{-3} , and test loss reaches a value of 2.3×10^{-3} .

The SPNN learns the integration scheme of the dynamics in the low manifold reached with the SAE. The input of the net are the latent variables, so the input size is 13. Providing that L and M are skew symmetric and symmetric, respectively, we only learn the upper elements of the main diagonal. Thus, instead of learning the full matrices of dimension $d \times d$, we learn $d \cdot (d - 1)/2$ elements for L and $d \cdot (d + 1)/2$ elements for M . Therefore, considering that the gradients have size d , the final output size is $d_{out} = d \cdot (d - 1)/2 + d \cdot (d + 1)/2 + d + d = 195$.

We have reduced the complexity of the dynamics thanks to the model order reduction applied. In spite of it, the dynamics and the latent evolution are still complicated for training. We require a structure of $N_h = 13$ hidden layers of size 195.

The SPNN has been also initialized following the Kaiming method. We have applied ReLU activations for hidden layers, and linear activations in the first and last layers. The initial parameters are set to $lr = 10^{-3}$, $wd = 10^{-5}$. The optimizer selected for training is also Adam, and the scheduler updates the learning rate after 1500, 2400, and 4000 epochs. Lower learning rates were required, again, due to the complexity of the features to be learnt. The weight assigned to the MSE loss is $\lambda_{mse}^{spnn} = 10^3$, to give more importance to the reconstruction.

We train the SPNN for 5000 epochs. At that point the training and test losses are 3.2×10^{-3} and 1.42×10^{-2} , respectively.

5.2 Initial validation

The performance of the method is tested with an input sequence extracted from the simulation of initial velocity 0.2 m/s. Given this sequence, the information is mapped to the latent state. Once we obtain the latent variables corresponding to that sequence, the SPNN integrates the dynamics until the fluid reaches the steady state. We could provide information of sequences at each time step, but data acquisition is not always accesible in real scenarios (occlusion, connection problems, ...). In those cases, the simulation should continue until new information is provided. To this end, we test the ability of the method to continue integrating and the stability of the simulation and results by providing only one snapshot as initial condition.

Table 2: Loss comparison among SAE, kPCA and POD

| | Error AE | Error POD | Error kPCA |
|----------|-----------------------|-----------------------|------------------------|
| q | 1.49×10^{-5} | 2.57×10^{-5} | 1.41×10^{-5} |
| v | 4.1×10^{-4} | 1.9×10^{-3} | 6.25×10^{-4} |
| e | 4.72×10^{-5} | 6.4×10^{-5} | 3.42×10^{-5} |
| σ | 5.1×10^{-4} | 2×10^{-3} | 3.371×10^{-4} |
| τ | 7.98×10^{-5} | 1.9×10^{-3} | 3.36×10^{-4} |

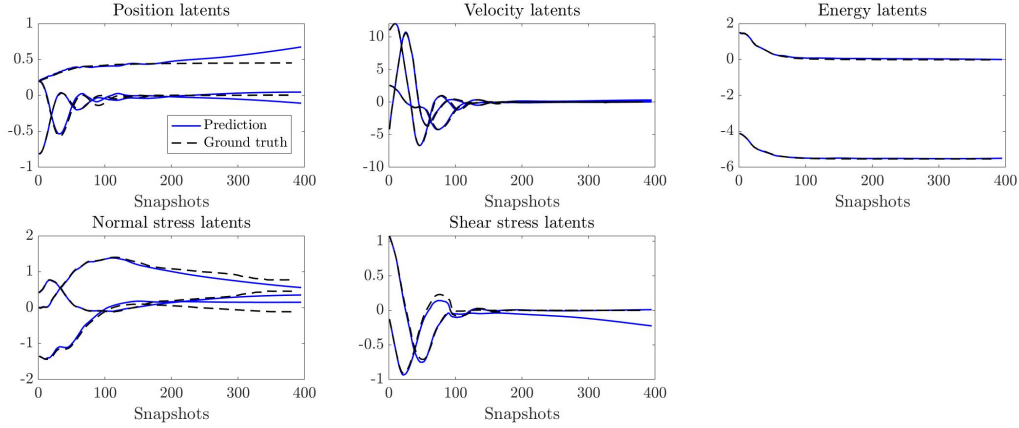


Figure 3: Simulation results. Learning of the dynamics in the latent manifold. Dashed lines represent the time evolution of the latents that aimed to be emulated. Lines in blue represent the result of the SPNN in the latent manifold.

Table 2 shows the MSE of the autoencoder proposed to reconstruct each group of state variables. These results have been compared with those obtained with POD [74] taking 10 modes, and kPCA [75] with 4 modes. Modes are selected with regard to the evolution of the eigenvalues obtained from each method. The AE achieves the same or improved levels of accuracy than POD and kPCA. Figure 3 plots the simulation results in the reduced-order space. The initial state has been projected to the latent manifold to emulate the evolution of its behavior. Fig. 5 plots the time evolution of some state variables in the high-dimensional space for 21 randomly selected particles. Finally, Fig. 4 shows the comparison between the ground truth and the projection of the results to the high order manifold at three time steps. This figure also includes the RMSE error of the reconstruction of each snapshot and the Hausdorff distance between the ground truth and the result. The Hausdorff distance (HD) [76] evaluates the closeness of two sets by analyzing the largest distance between one set of points to other. If the HD is low, it resembles a high degree of similarity

$$HD = \max\left\{\sup_{x \in X} d(x, Y), \sup_{y \in Y} d(y, X)\right\},$$

being X and Y the two sets to be compared. After analyzing the results obtained in the computational phase, we decide to test the loop in a real scenario for reconstruction of real fluids.

6 Tests with real-world data

Once the proposed strategy has been tested on computational data, it is extended to real-world problems. A RGBD camera is used to track the free surface of the fluid. This information is converted into sequences to predict the next state of the fluid. Finally, we have not only a reconstruction, but an augmented representation of the fluid providing velocity, internal energy and stress fields.

6.1 Data acquisition review

Firstly, we need to detect the free surface of the fluid and perform measurements to feed the algorithm with real data. We make use of a stereo camera for this purpose, although many of the presented results could equally be obtained



Figure 4: Comparison of the reconstruction of the integration provided by the SPNN (right) with the ground truth (left). The selected snapshots correspond to peaks of the sloshing dynamics of glycerine. Specifically we present the comparison for snapshots 1, 33 and 64 of the collection.

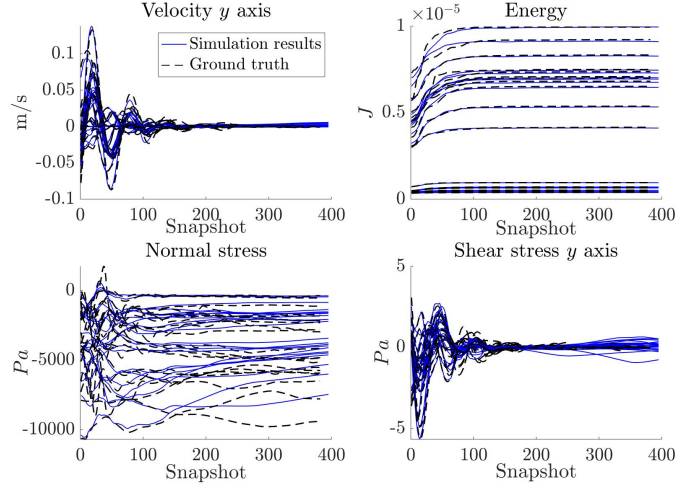


Figure 5: Time evolution of selected state variables evaluated at 21 random particles. The graph shows a comparison between the simulated fields with the ground truth for the validation simulation of the algorithm.

with a standard camera. The model of our stereo camera is RealSense D415 (<https://www.intelrealsense.com/depth-camera-d415/>). This model of stereo camera provides both intrinsic and extrinsic parameters as well as depth measurements. Thus, the projection of the 2D to the 3D, and viceversa, is straight forward. The free surface is detected with regard to the pixel coordinates of each point u, v . The software provides the intrinsic parameters f_x, f_y, c_x, c_y, s , which are the focal length, the optical center coordinates and the skew coefficient respectively. In addition to the intrinsic parameters K , we can also estimate (by means of Simultaneous Localization and Mapping techniques [77]), the rotation R and translation t components to complete the projection to the real world coordinates X, Y, Z of the point p_w ,

$$s \begin{bmatrix} u \\ v \\ 1 \end{bmatrix} = \begin{bmatrix} f_x & 0 & c_x \\ 0 & f_y & c_y \\ 0 & 0 & 1 \end{bmatrix} \begin{bmatrix} r_{11} & r_{12} & r_{13} & t_1 \\ r_{21} & r_{22} & r_{23} & t_2 \\ r_{31} & r_{32} & r_{33} & t_3 \end{bmatrix} \begin{bmatrix} X \\ Y \\ Z \\ 1 \end{bmatrix},$$

$$\tilde{\mathbf{x}}_s = \mathbf{K}[\mathbf{R}|\mathbf{t}]\mathbf{p}_w.$$

A sketch of the camera system is depicted in Fig. 6.

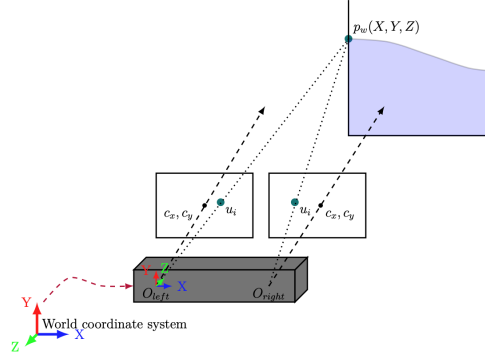


Figure 6: Representation of the data acquisition system. The free surface is the tracked element of the algorithm to perform learning and the simulation of the dynamics.

It is worth mentioning that the original frame does not provide good enough depth measurements. It reports holes where the algorithm did not successfully measure the depth of the pixels. Measurements related to transparent objects are often invalid or noisy since their surfaces are not Lambertian, which is the main assumption of the measurement algorithm incorporated in the stereo camera. In other words, instead of reflecting light evenly in all directions they also refract light, resulting in unmeasurable conditions for the technique defined. Our approach consists in applying some filters to enhance the depth streaming. Firstly, we apply a decimation filter to reduce the complexity of the measurements to foster stability. Then, the frame is mapped to a disparity map where the spatial filter, to preserve the edges, and the temporal filter, to promote data persistency, are applied. This result is projected back to the depth map where the hole-filling filter is finally applied. The filtered depth map outputs a full depth field from which we can evaluate the position of the glass and the free surface (see Fig. 7). This procedure is fully detailed in the reference [78].



Figure 7: Color and depth stream before (up) and after (down) applying the required filters to reconstruct the depth map of the streaming.

We binarize the color frame, also streamed by the camera, to convert the image into a black and white picture. The free surface appears as a gradient in the black and white image, see Fig. 8. Since we value the speed in the data streaming, we define an area for performing these analysis instead of forcing the recognition across the full image. The points of the free surface are detected, tracked, projected from frame coordinates to 3D, and stored.

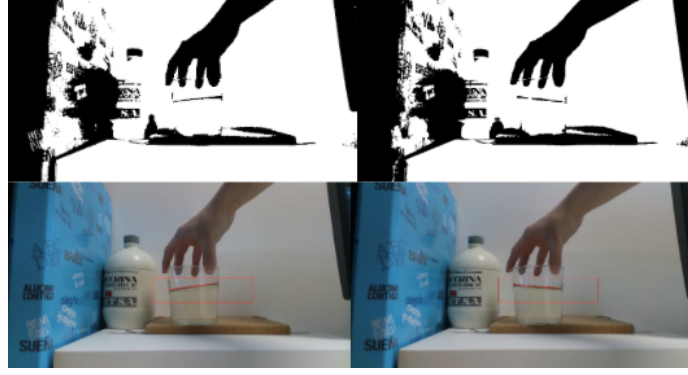


Figure 8: Representation of the color frame and its conversion to a binarized image to seek the free surface. The area defined for searching is represented in the color frame as well as the points of the free surface detected in the black and white image.

6.2 Reconstruction and integration from video streaming

We assemble the data obtained from the data acquisition step into sequences. These sequences feed the algorithm trained with computational data. The RNN projects the sequences to the latent space, the SPNN integrates the dynamics, and the decoder projects back not only the next state of the free surface, but also the position of the whole set of particles as well the velocity, internal energy, σ and τ . Therefore, we reconstruct the complete state of the fluid at the next time step only from the free surface. Video stream for validation consists of 800 frames, which is a recording of 12 seconds.

Figure 10 shows the results of the algorithm compared to the real video streaming. We perform the reconstruction and integration over the whole sequence, i.e. no cuts were applied to the streaming and the method is applied continuously. We apply the three steps (RNN projection, integration, and decoding) over the full video in 3.42 seconds on an ordinary laptop (Macbook Pro 2013-3 GHz Intel Core i7), achieving (much more than) the real-time performance proposed. Some snapshots of a sloshing phenomenon were selected and plotted in the first row of Fig. 6.2. The snapshots shown represent the peaks, which are the most critical states in manipulation, and some intermediate states between the peaks. The rest of pictures correspond to the augmented information obtained with this method, that has been possible thanks to the physics-aware simulation framework.

All results of the integration are stable, realistic, and close to the real result. We analyze objectively the results by evaluating the root mean squared error (RMSE) between the real \mathbf{y} and the predicted $\hat{\mathbf{y}}$ free surfaces in n snapshots of the video streaming. In other words, we feed the algorithm with the free surface in t (from the video), and we compare the integration result ($t + 1$) with the free surface in $t + 1$ (from the video),

$$\text{RMSE} = \sqrt{\frac{1}{n} \sum_{t=1}^n (\hat{\mathbf{y}}_t - \mathbf{y}_t)^2}.$$

The evolution of the error along the video is represented in Fig. 11. The error remains under 5 mm in the whole sequence of the length of the video, and stays lower than 3 mm in the vast majority of it. We also evaluate the HD between the free surface that comes from the camera and the simulation. These results resemble the closeness between the free surfaces, for which there is not a larger deviation than 4–5 mm even in the higher peaks of the sloshing.

In some cases, higher deviations in the HD come from distortions in the detection of the free surface (like in the first snapshot of water presented).

Fig. 12 showcases finally the compliance of the principles of the thermodynamics in the predictions. The time derivative of energy makes little oscillations due to the numerical approximation around 0, which means that we ensure the conservation of energy. In addition, the time derivative of entropy remains always positive, fulfilling its production.

7 Conclusions and future work

We have presented an approach for physical perception of sloshing phenomena. It is based upon physics-informed learned simulators connected to the real world by means of commodity RGBD cameras. The algorithm has been

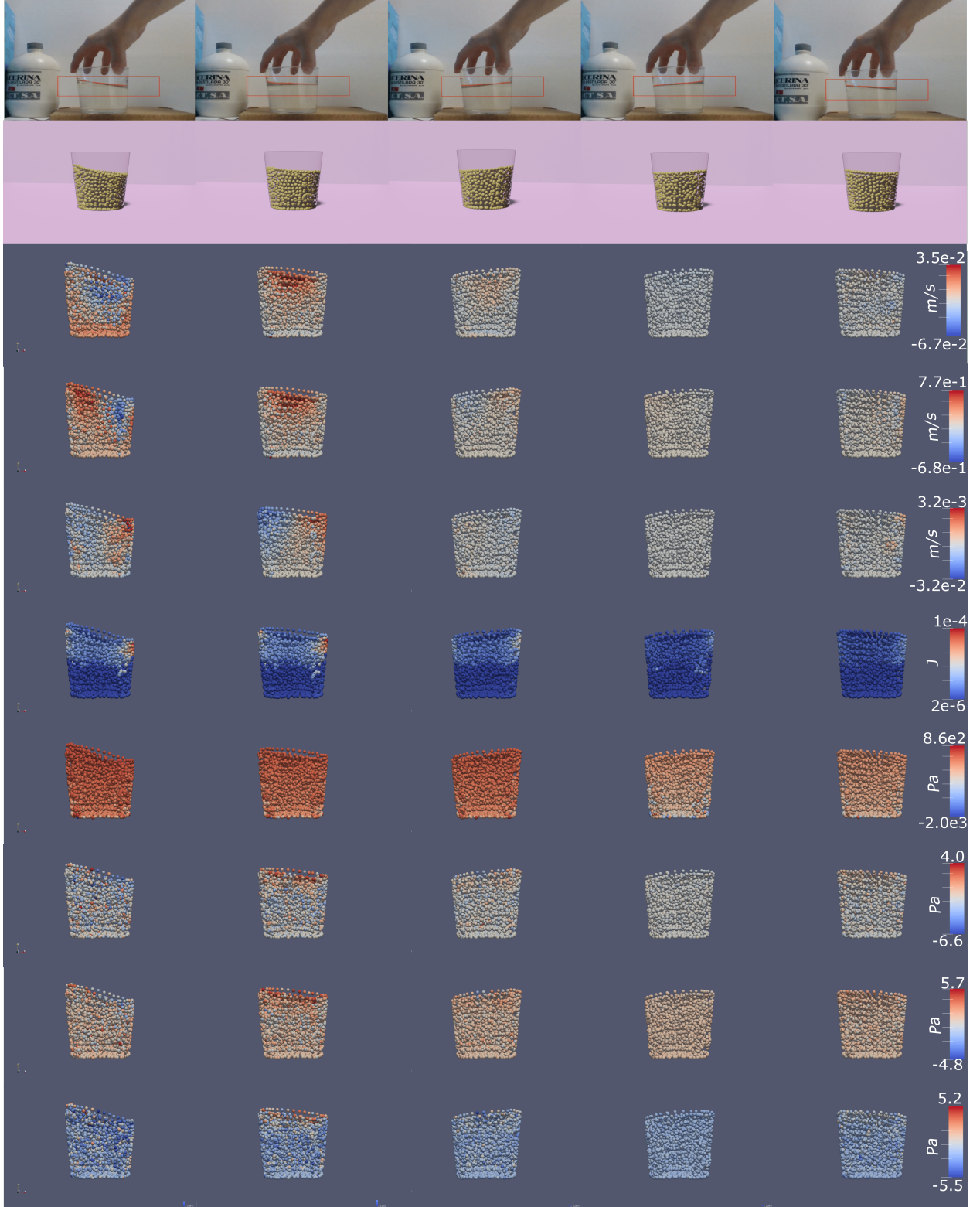


Figure 9: Results for a 12 seconds video of a glass of glycerine. Eight snapshots of the sloshing sequence were selected for comparison. The selected snapshots have index 560, 565, 568, 572, 578 from left to right. The second row corresponds to the fluid reconstruction and prediction provided the previous snapshot. From row three to ten we show the additional information obtained from the reconstruction and simulation (velocity, energy and stress fields, respectively).

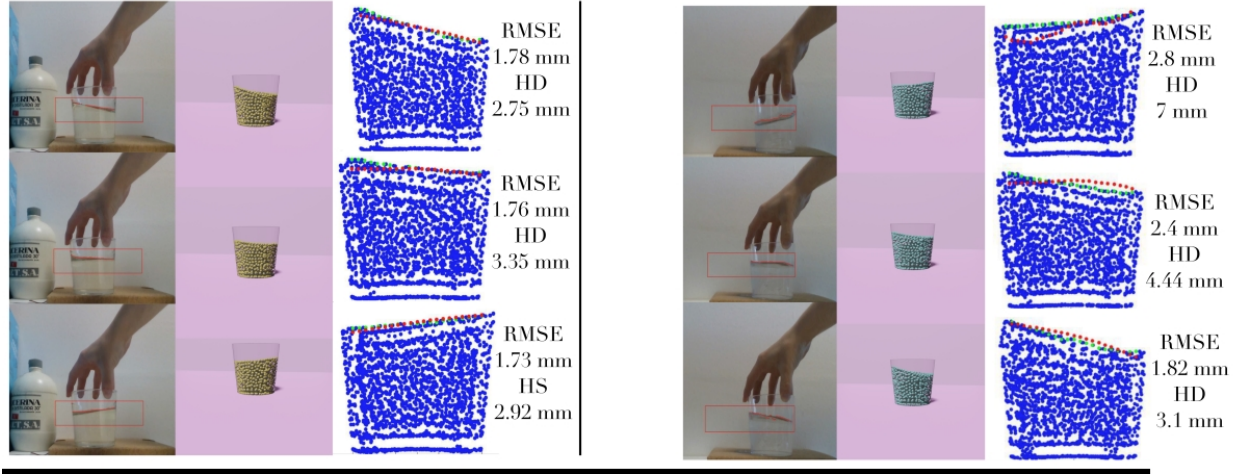


Figure 10: Detail of the comparison of glycerine (left) and water (right) with the prediction. The third column of both liquids compares the predicted fluid volume (in blue), the free surface of the liquid volume (green) and the target free surface (in red). The RMSE and the Hausdorff distance (HD) that correspond to each snapshot are indicated.

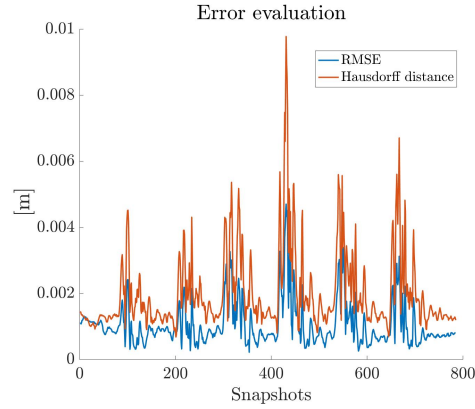


Figure 11: Evolution of the mean squared error during the perception process of sloshing in a glass of glycerine.

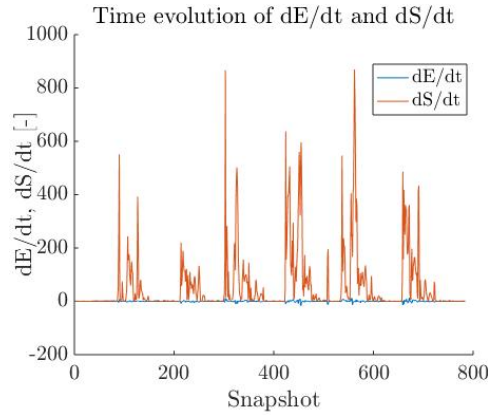


Figure 12: Time derivatives of energy and Entropy along the video. The time derivative of Energy oscillates around zero, ensuring energy conservation. Entropy production is also ensured since the time derivative is always positive.

trained with computational data to build a physically sound reduced-order manifold to learn the evolution of the dynamics dictated by the General Equation for the Non-Equilibrium Reversible-Irreversible Coupling (GENERIC). This thermodynamic framework ensures the physical consistency, accuracy and realism of the results to promote informed decision making.

Provided the physics-aware approach for learning, only four simulations per fluid were needed to perform a training that accurately mimics computational and real behaviors. This approach has been completed with the development of a self-supervised technique to recover information of the dynamics that is unmeasurable by ordinary means. Despite the existence of sensors and advanced tools, such as PIV cameras, for evaluating data that cannot be extracted from simple video streamings, we are still unable to evaluate important information for a complete physical description. The suggested methodology fills in the gaps of information for the simulation of future dynamical states.

Since the main purpose of the approach is to connect real-world systems with AI-guided simulators, we test the implementation of the integration scheme with a data-acquisition system. The free surface is tracked by a RGBD camera, and the information obtained is used for fluid prediction. Notably, real-time is successfully achieved due to the reduction obtained through the application of autoencoders: 12 seconds of real-world time are analyzed in slightly more than 3 seconds, thus allowing performing decision making or using control algorithms. In addition, information is provided to the user by using augmented reality, i.e., by outputting the reconstructed fluid volume and a set of variables that may be important for decision making on top of the video stream.

Nonetheless, physics perception must achieve generality. It is unmanageable to train a model for each casuistic. Consequently, transfer learning must be extended to world and scene reasoning. Starting from a model such as the one proposed, incremental learning could set the base to extend learning and build hybrid twins that learn from evolving scenarios. Finally, the permutation-invariant condition is a desirable characteristic to work with unordered meshes [79] [80] [81]. The consideration of this condition would help to achieve a higher degree of adaptivity and complexity previewed in future works.

Acknowledgments

The work presented has been partially supported by the Spanish Ministry of Economy and Competitiveness through Grant number PID2020-113463RB-C31 and by the Regional Government of Aragon and the European Social Fund, research group T88. The authors also thank the support of ESI Group through the project UZ-2019-0060.

References

- [1] C. K. Liu and D. Negrut, “The role of physics-based simulators in robotics,” *Annual Review of Control, Robotics, and Autonomous Systems*, vol. 4, 2020.
- [2] C. J. Bates, I. Yildirim, J. B. Tenenbaum, and P. Battaglia, “Modeling human intuitions about liquid flow with particle-based simulation,” *PLoS computational biology*, vol. 15, no. 7, p. e1007210, 2019.
- [3] P. W. Battaglia, J. B. Hamrick, and J. B. Tenenbaum, “Simulation as an engine of physical scene understanding,” *Proceedings of the National Academy of Sciences*, vol. 110, no. 45, pp. 18 327–18 332, 2013.
- [4] C. Schenck and D. Fox, “Spnets: Differentiable fluid dynamics for deep neural networks,” in *Conference on Robot Learning*. PMLR, 2018, pp. 317–335.
- [5] L. Li, S. Hoyer, R. Pederson, R. Sun, E. D. Cubuk, P. Riley, K. Burke *et al.*, “Kohn-sham equations as regularizer: Building prior knowledge into machine-learned physics,” *Physical review letters*, vol. 126, no. 3, p. 036401, 2021.
- [6] M. Raissi, P. Perdikaris, and G. E. Karniadakis, “Physics informed deep learning (part i): Data-driven solutions of nonlinear partial differential equations,” *arXiv preprint arXiv:1711.10561*, 2017.
- [7] L. Yang, X. Meng, and G. E. Karniadakis, “B-pinns: Bayesian physics-informed neural networks for forward and inverse pde problems with noisy data,” *Journal of Computational Physics*, vol. 425, p. 109913, 2021.
- [8] Z. Liu and M. Tegmark, “AI Poincaré: Machine Learning Conservation Laws from Trajectories,” *arXiv preprint arXiv:2011.04698*, 2020.
- [9] K. L. Course, T. W. Evans, and P. B. Nair, “Weak form generalized hamiltonian learning,” *arXiv preprint arXiv:2104.05096*, 2021.
- [10] Z. Bai, S. L. Brunton, B. W. Brunton, J. N. Kutz, E. Kaiser, A. Spohn, and B. R. Noack, “Data-driven methods in fluid dynamics: Sparse classification from experimental data,” in *Whither Turbulence and Big Data in the 21st Century?* Springer, 2017, pp. 323–342.

- [11] P. Rodríguez-Ocampo, M. Ring, J. Hernandez-Fontes, J. Alcérreca-Huerta, E. Mendoza, G. Gallegos-Diez-Barroso, and R. Silva, “A 2d image-based approach for cfd validation of liquid mixing in a free-surface condition,” *Journal of Applied Fluid Mechanics*, vol. 13, no. 5, 2020.
- [12] K. Bieker, S. Peitz, S. L. Brunton, J. N. Kutz, and M. Dellnitz, “Deep model predictive flow control with limited sensor data and online learning,” *Theoretical and Computational Fluid Dynamics*, pp. 1–15, 2020.
- [13] A. Sancarlos, M. Cameron, A. Abel, E. Cueto, J.-L. Duval, and F. Chinesta, “From rom of electrochemistry to ai-based battery digital and hybrid twin,” *Archives of Computational Methods in Engineering*, vol. 28, no. 3, pp. 979–1015, 2021.
- [14] B. Moya, I. Alfaro, D. Gonzalez, F. Chinesta, and E. Cueto, “Physically sound, self-learning digital twins for sloshing fluids,” *PLoS One*, vol. 15, no. 6, p. e0234569, 2020.
- [15] M. Grmela and H. C. Öttinger, “Dynamics and thermodynamics of complex fluids. i. development of a general formalism,” *Physical Review E*, vol. 56, no. 6, p. 6620, 1997.
- [16] P. W. Battaglia, J. B. Hamrick, V. Bapst, A. Sanchez-Gonzalez, V. Zambaldi, M. Malinowski, A. Tacchetti, D. Raposo, A. Santoro, R. Faulkner *et al.*, “Relational inductive biases, deep learning, and graph networks,” *arXiv preprint arXiv:1806.01261*, 2018.
- [17] A. Nair, D. Chen, P. Agrawal, P. Isola, P. Abbeel, J. Malik, and S. Levine, “Combining self-supervised learning and imitation for vision-based rope manipulation,” in *2017 IEEE international conference on robotics and automation (ICRA)*. IEEE, 2017, pp. 2146–2153.
- [18] M. Nava, A. Paolillo, J. Guzzi, L. M. Gambardella, and A. Giusti, “Uncertainty-aware self-supervised learning of spatial perception tasks,” *arXiv preprint arXiv:2103.12007*, 2021.
- [19] M. Yan, Y. Zhu, N. Jin, and J. Bohg, “Self-supervised learning of state estimation for manipulating deformable linear objects,” *IEEE robotics and automation letters*, vol. 5, no. 2, pp. 2372–2379, 2020.
- [20] C. Rao, H. Sun, and Y. Liu, “Physics-informed deep learning for computational elastodynamics without labeled data,” *Journal of Engineering Mechanics*, vol. 147, no. 8, p. 04021043, 2021.
- [21] J. L. Callahan, K. Maeda, and S. L. Brunton, “Robust flow reconstruction from limited measurements via sparse representation,” *Physical Review Fluids*, vol. 4, no. 10, p. 103907, 2019.
- [22] L. Sun and J.-X. Wang, “Physics-constrained bayesian neural network for fluid flow reconstruction with sparse and noisy data,” *Theoretical and Applied Mechanics Letters*, vol. 10, no. 3, pp. 161–169, 2020.
- [23] N. B. Erichson, L. Mathelin, Z. Yao, S. L. Brunton, M. W. Mahoney, and J. N. Kutz, “Shallow neural networks for fluid flow reconstruction with limited sensors,” *Proceedings of the Royal Society A*, vol. 476, no. 2238, p. 20200097, 2020.
- [24] K. O. Lye, S. Mishra, and D. Ray, “Deep learning observables in computational fluid dynamics,” *Journal of Computational Physics*, vol. 410, p. 109339, 2020.
- [25] Y. LeCun, Y. Bengio, and G. Hinton, “Deep learning,” *nature*, vol. 521, no. 7553, pp. 436–444, 2015.
- [26] A. K. Maier, C. Syben, B. Stimpel, T. Würfl, M. Hoffmann, F. Schebesch, W. Fu, L. Mill, L. Kling, and S. Christiansen, “Learning with known operators reduces maximum error bounds,” *Nature Machine Intelligence*, vol. 1, no. 8, pp. 373–380, 2019. [Online]. Available: <https://doi.org/10.1038/s42256-019-0077-5>
- [27] B. Lusch, J. N. Kutz, and S. L. Brunton, “Deep learning for universal linear embeddings of nonlinear dynamics,” *Nature communications*, vol. 9, no. 1, pp. 1–10, 2018.
- [28] J. Ayensa-Jiménez, M. H. Doweidar, J. A. Sanz-Herrera, and M. Doblaré, “Prediction and identification of physical systems by means of physically-guided neural networks with meaningful internal layers,” *Computer Methods in Applied Mechanics and Engineering*, vol. 381, p. 113816, 2021.
- [29] P. Jin, Z. Zhang, I. G. Kevrekidis, and G. E. Karniadakis, “Learning poisson systems and trajectories of autonomous systems via poisson neural networks,” *arXiv preprint arXiv:2012.03133*, 2020.
- [30] J. S. Hesthaven, C. Pagliantini, and N. Ripamonti, “Rank-adaptive structure-preserving reduced basis methods for hamiltonian systems,” *arXiv preprint arXiv:2007.13153*, 2020.
- [31] F. Masi, I. Stefanou, P. Vannucci, and V. Maffi-Berthier, “Material modeling via thermodynamics-based artificial neural networks,” in *Workshop on Joint Structures and Common Foundations of Statistical Physics, Information Geometry and Inference for Learning*. Springer, 2020, pp. 308–329.
- [32] H. Yu, X. Tian, Q. Li *et al.*, “OnsagerNet: Learning stable and interpretable dynamics using a generalized onsager principle,” *arXiv preprint arXiv:2009.02327*, 2020.

- [33] R. Ibañez, D. Borzacchiello, J. V. Aguado, E. Abisset-Chavanne, E. Cueto, P. Ladeveze, and F. Chinesta, “Data-driven non-linear elasticity: constitutive manifold construction and problem discretization,” *Computational Mechanics*, vol. 60, no. 5, pp. 813–826, 2017.
- [34] D. González, F. Chinesta, and E. Cueto, “Thermodynamically consistent data-driven computational mechanics,” *Continuum Mechanics and Thermodynamics*, vol. 31, no. 1, pp. 239–253, 2019.
- [35] —, “Learning non-markovian physics from data,” *Journal of Computational Physics*, vol. 428, p. 109982, 2021.
- [36] C. Ghnatios, I. Alfaro, D. González, F. Chinesta, and E. Cueto, “Data-driven generic modeling of poroviscoelastic materials,” *Entropy*, vol. 21, no. 12, p. 1165, 2019.
- [37] B. Moya, D. González, I. Alfaro, F. Chinesta, and E. Cueto, “Learning slosh dynamics by means of data,” *Computational Mechanics*, vol. 64, no. 2, pp. 511–523, 2019.
- [38] Q. Hernandez, A. Badías, D. González, F. Chinesta, and E. Cueto, “Deep learning of thermodynamics-aware reduced-order models from data,” *Computer Methods in Applied Mechanics and Engineering*, vol. 379, p. 113763, 2021.
- [39] Q. Hernandez, A. Badías, D. González, F. Chinesta, and E. Cueto, “Structure-preserving neural networks,” *Journal of Computational Physics*, vol. 426, p. 109950, 2021.
- [40] B. Kim, V. C. Azevedo, N. Thuerey, T. Kim, M. Gross, and B. Solenthaler, “Deep fluids: A generative network for parameterized fluid simulations,” in *Computer Graphics Forum*, vol. 38, no. 2. Wiley Online Library, 2019, pp. 59–70.
- [41] J. Tompson, K. Schlachter, P. Sprechmann, and K. Perlin, “Accelerating eulerian fluid simulation with convolutional networks,” in *International Conference on Machine Learning*. PMLR, 2017, pp. 3424–3433.
- [42] T. P. Miyanawala and R. K. Jaiman, “An efficient deep learning technique for the navier-stokes equations: Application to unsteady wake flow dynamics,” *arXiv preprint arXiv:1710.09099*, 2017.
- [43] S. R. Bukka, R. Gupta, A. R. Magee, and R. K. Jaiman, “Assessment of unsteady flow predictions using hybrid deep learning based reduced-order models,” *Physics of Fluids*, vol. 33, no. 1, p. 013601, 2021.
- [44] S. Wiewel, M. Becher, and N. Thuerey, “Latent space physics: Towards learning the temporal evolution of fluid flow,” in *Computer graphics forum*, vol. 38, no. 2. Wiley Online Library, 2019, pp. 71–82.
- [45] A. Sanchez-Gonzalez, J. Godwin, T. Pfaff, R. Ying, J. Leskovec, and P. Battaglia, “Learning to simulate complex physics with graph networks,” in *International Conference on Machine Learning*. PMLR, 2020, pp. 8459–8468.
- [46] Z. Mao, A. D. Jagtap, and G. E. Karniadakis, “Physics-informed neural networks for high-speed flows,” *Computer Methods in Applied Mechanics and Engineering*, vol. 360, p. 112789, 2020.
- [47] H. Gao, L. Sun, and J.-X. Wang, “Phygeonet: physics-informed geometry-adaptive convolutional neural networks for solving parameterized steady-state pdes on irregular domain,” *Journal of Computational Physics*, vol. 428, p. 110079, 2021.
- [48] Y. Li, T. Lin, K. Yi, D. Bear, D. Yamins, J. Wu, J. Tenenbaum, and A. Torralba, “Visual grounding of learned physical models,” in *International Conference on Machine Learning*. PMLR, 2020, pp. 5927–5936.
- [49] J. Wu, I. Yildirim, J. J. Lim, B. Freeman, and J. Tenenbaum, “Galileo: Perceiving physical object properties by integrating a physics engine with deep learning,” *Advances in neural information processing systems*, vol. 28, pp. 127–135, 2015.
- [50] C. Schenck and D. Fox, “Perceiving and reasoning about liquids using fully convolutional networks,” *The International Journal of Robotics Research*, vol. 37, no. 4-5, pp. 452–471, 2018.
- [51] J. J. Monaghan, “Smoothed particle hydrodynamics,” *Annual review of astronomy and astrophysics*, vol. 30, no. 1, pp. 543–574, 1992.
- [52] S. J. Koppal, *Lambertian Reflectance*. Boston, MA: Springer US, 2014, pp. 441–443. [Online]. Available: https://doi.org/10.1007/978-0-387-31439-6_534
- [53] C. Schenck and D. Fox, “Detection and tracking of liquids with fully convolutional networks,” *arXiv preprint arXiv:1606.06266*, 2016.
- [54] C. Do, T. Schubert, and W. Burgard, “A probabilistic approach to liquid level detection in cups using an rgb-d camera,” in *2016 IEEE/RSJ International Conference on Intelligent Robots and Systems (IROS)*. IEEE, 2016, pp. 2075–2080.
- [55] S. Eppel, “Tracing liquid level and material boundaries in transparent vessels using the graph cut computer vision approach,” *arXiv preprint arXiv:1602.00177*, 2016.

- [56] T. Bertalan, F. Dietrich, I. Mezić, and I. G. Kevrekidis, “On learning hamiltonian systems from data,” *Chaos: An Interdisciplinary Journal of Nonlinear Science*, vol. 29, no. 12, p. 121107, 2019.
- [57] S. Greydanus, M. Dzamba, and J. Yosinski, “Hamiltonian neural networks,” in *Advances in Neural Information Processing Systems*, 2019, pp. 15 379–15 389.
- [58] P. Jin, A. Zhu, G. E. Karniadakis, and Y. Tang, “Symplectic networks: Intrinsic structure-preserving networks for identifying hamiltonian systems,” *arXiv preprint arXiv:2001.03750*, 2020.
- [59] P. Toth, D. J. Rezende, A. Jaegle, S. Racanière, A. Botev, and I. Higgins, “Hamiltonian generative networks,” *arXiv preprint arXiv:1909.13789*, 2019.
- [60] Y. D. Zhong, B. Dey, and A. Chakraborty, “Symplectic ode-net: Learning hamiltonian dynamics with control,” *arXiv preprint arXiv:1909.12077*, 2019.
- [61] P. Español, *Statistical Mechanics of Coarse-Graining*. Berlin, Heidelberg: Springer Berlin Heidelberg, 2004, pp. 69–115. [Online]. Available: http://dx.doi.org/10.1007/978-3-540-39895-0_3
- [62] R. Kubo, “The fluctuation-dissipation theorem,” *Reports on progress in physics*, vol. 29, no. 1, p. 255, 1966.
- [63] P. Espanol, M. Serrano, and H. C. Öttinger, “Thermodynamically admissible form for discrete hydrodynamics,” *Physical review letters*, vol. 83, no. 22, p. 4542, 1999.
- [64] K. Taira, M. S. Hemati, S. L. Brunton, Y. Sun, K. Duraisamy, S. Bagheri, S. T. Dawson, and C.-A. Yeh, “Modal analysis of fluid flows: Applications and outlook,” *AIAA journal*, vol. 58, no. 3, pp. 998–1022, 2020.
- [65] N. B. Erichson, M. Muehlebach, and M. W. Mahoney, “Physics-informed autoencoders for lyapunov-stable fluid flow prediction,” *arXiv preprint arXiv:1905.10866*, 2019.
- [66] A. Ng *et al.*, “Sparse autoencoder,” *CS294A Lecture notes*, vol. 72, no. 2011, pp. 1–19, 2011.
- [67] R. Pascanu, T. Mikolov, and Y. Bengio, “On the difficulty of training recurrent neural networks,” in *International conference on machine learning*. PMLR, 2013, pp. 1310–1318.
- [68] K. Cho, B. Van Merriënboer, C. Gulcehre, D. Bahdanau, F. Bougares, H. Schwenk, and Y. Bengio, “Learning phrase representations using rnn encoder-decoder for statistical machine translation,” *arXiv preprint arXiv:1406.1078*, 2014.
- [69] S. Hochreiter and J. Schmidhuber, “Long short-term memory,” *Neural computation*, vol. 9, no. 8, pp. 1735–1780, 1997.
- [70] J. Chung, C. Gulcehre, K. Cho, and Y. Bengio, “Empirical evaluation of gated recurrent neural networks on sequence modeling,” *arXiv preprint arXiv:1412.3555*, 2014.
- [71] E. Celledoni, M. J. Ehrhardt, C. Etmann, R. I. McLachlan, B. Owren, C.-B. Schönlieb, and F. Sherry, “Structure preserving deep learning,” *arXiv preprint arXiv:2006.03364*, 2020.
- [72] M. Smith, ABAQUS/Standard User’s Manual, Version 6.9. United States: Dassault Systèmes Simulia Corp, 2009.
- [73] K. He, X. Zhang, S. Ren, and J. Sun, “Delving deep into rectifiers: Surpassing human-level performance on imagenet classification,” in *Proceedings of the IEEE international conference on computer vision*, 2015, pp. 1026–1034.
- [74] H. V. Ly and H. T. Tran, “Modeling and control of physical processes using proper orthogonal decomposition,” *Mathematical and computer modelling*, vol. 33, no. 1-3, pp. 223–236, 2001.
- [75] B. Schölkopf, A. Smola, and K.-R. Müller, “Nonlinear component analysis as a kernel eigenvalue problem,” *Neural computation*, vol. 10, no. 5, pp. 1299–1319, 1998.
- [76] D. P. Huttenlocher, G. A. Klanderman, and W. J. Rucklidge, “Comparing images using the hausdorff distance,” *IEEE Transactions on pattern analysis and machine intelligence*, vol. 15, no. 9, pp. 850–863, 1993.
- [77] R. Mur-Artal and J. D. Tardós, “Orb-slam2: An open-source slam system for monocular, stereo, and rgb-d cameras,” *IEEE Transactions on Robotics*, vol. 33, no. 5, pp. 1255–1262, 2017.
- [78] D. T. Anders Grunnet-Jepsen, “Depth post-processing for intel® realsense™ depth camera d400 series.”
- [79] C. R. Qi, L. Yi, H. Su, and L. J. Guibas, “Pointnet++: Deep hierarchical feature learning on point sets in a metric space,” *arXiv preprint arXiv:1706.02413*, 2017.
- [80] Y. Wang, Y. Sun, Z. Liu, S. E. Sarma, M. M. Bronstein, and J. M. Solomon, “Dynamic graph cnn for learning on point clouds,” *Acm Transactions On Graphics (tog)*, vol. 38, no. 5, pp. 1–12, 2019.
- [81] Y. Zhou and O. Tuzel, “Voxelnet: End-to-end learning for point cloud based 3d object detection,” in *Proceedings of the IEEE conference on computer vision and pattern recognition*, 2018, pp. 4490–4499.